Monthly Notices of the ROYAL ASTRONOMICAL SOCIETY

MNRAS **521,** L17–L23 (2023) https://doi.org/10.1093/mnrasl/slad020
Advance Access publication 2023 February 14

Evolution of rotating 25 $M_{\odot}$ Population III star: physical properties and resulting supernovae

Amar Aryan [1,2]★ Shashi Bhushan Pandey,[1] Rahul Gupta[1,2] and Amit Kumar Ror[1]

[1]*Aryabhatta Research Institute of Observational Sciences (ARIES), Manora Peak, Nainital 263002, India*
[2]*Department of Physics, Deen Dayal Upadhyaya Gorakhpur University, Gorakhpur 273009, India*

Accepted 2023 February 10. Received 2023 February 9; in original form 2022 December 14

ABSTRACT

In this letter, we report the outcomes of 1D modelling of a rotating 25 $M_{\odot}$ zero-age main sequence Population III (Pop III) star up to the stage of the onset of core collapse. Rapidly rotating models display violent and sporadic mass-losses after the main-sequence stage. In comparison to the solar metallicity model, Pop III models show very small pre-supernova radii. Further, with models at the stage of the onset of core collapse, we simulate the hydrodynamic simulations of resulting supernovae. Depending upon the mass-losses due to corresponding rotations and stellar winds, the resulting supernovae span a class from weak Type II to Type Ib/c. We find that the absolute magnitudes of the core-collapse supernovae resulting from Pop III stars are much fainter than that resulting from a solar metallicity star. From our simulation results, we also conclude that within the considered limits of explosion energies and nickel masses, these transient events are very faint, making it difficult for them to be detected at high-redshifts.

Key words: software: simulations – stars: neutron – stars: Population III – supernovae: general.

1 INTRODUCTION

The first generations of stars formed out of uncontaminated matter, initially comprised only of the first two stable elements, hydrogen (H) and helium (He) from the periodic table, are considered as the Population III (Pop III) stars. Due to the insufficiency of coolants in the primordial gas, it is hypothesized that the Pop III stars were massive intrinsically (Silk 1983; Tegmark et al. 1997; Bromm, Coppi & Larson 1999; Nakamura & Umemura 2001; Abel, Bryan & Norman 2002; Brook et al. 2007; Salvadori et al. 2010; Hirano et al. 2015). However, there have been multiple studies to apprehend the possibility of the existence of Pop III stars having low masses. In recent simulations, it has been found that the formation of pristine, metal-free stars at low to intermediate masses could potentially be due to the fragmented accretion discs around massive Pop III protostars (Turk, Abel & O'Shea 2009; Stacy, Greif & Bromm 2010; Clark et al. 2011; Hosokawa et al. 2011; Greif et al. 2012; Hirano et al. 2014, 2015; Stacy, Bromm & Lee 2016; Riaz et al. 2018; Wollenberg et al. 2020). On the low-mass Pop III stars, Ishiyama et al. (2016) have found that the Pop III stars having masses $< 0.8\,M_{\odot}$ would have longer lifetimes as compared to the cosmic time therefore such low-mass stars could linger around to be detected in our Milky Way itself.

Further, Pop III stars were responsible for the enrichment of the early universe by spreading metals heavier than He through violent supernova (SN) explosions or possibly through sporadic mass-losses due to vigorous stellar winds (Ferrara, Pettini & Shchekinov 2000; Abia et al. 2001). The study by Chiaki, Susa & Hirano (2018) shows that a core-collapse supernova (CCSN) from a Pop III star could cause the mini halo to undergo internal-enrichment. This causes the metallicity to be $-5 \lesssim$ [Fe/H] $\lesssim -3$ in the recollapsing region. Thus, internal-enrichment caused by a CCSN from a Pop III star can explain the stars which are extremely metal poor. In a relatively recent work, the authors of Kirihara et al. (2020) have estimated the dose of heavy elements introduced by massive Pop III stars. In doing so, they considered the amount of heavy elements synthesized only from pair-instability supernovae (PISNe) or CCSNe explosions of massive Pop III stars. They found that the heavy elements introduced by Pop III stars are usually much more than those from galaxies found in the low-density regions. Besides the above-mentioned studies involving Pop III stars, there have also been investigations to recognize the influence of Pop III stars on cosmic reionization (e.g. Haiman, Rees & Loeb 1997; Tumlinson & Shull 2000; Barkana & Loeb 2001; Ciardi et al. 2001; Bromm 2013), and dust formation (Todini & Ferrara 2001).

There have been multiple studies to understand the evolution of the Pop III stars. Marigo, Chiosi & Kudritzki (2003) and Ekström et al. (2008) have studied the evolution of Pop III stars by assuming solid body and differential rotation, respectively. Heger & Woosley (2010) have discussed the nucleosynthesis and evolutions of non-rotating Pop III stars. They also generated the light curves of the resulting transients from the non-rotating models corresponding to different explosion energies. Yoon, Dierks & Langer (2012) have discussed the evolution of massive Pop III stars having masses in the range of [10–1000] $M_{\odot}$ and have investigated the consequences of including rotation and magnetic fields. Due to the chemically homogeneous evolution, the rapidly rotating high-mass stars could result into a class of energetic transients including Type Ib/c SNe, gamma-ray bursts, hypernovae, and PISNe. In their work, Yoon et al.

★ E-mail: amararyan941@gmail.com, amar@aries.res.in

(2012) have prepared a phase diagram in the plane of mass and rotational velocity at zero-age main sequence (ZAMS) and discussed the culminating fates of Pop III stars. The authors of Windhorst et al. (2018) have investigated the evolutions of non-rotating Pop III stars in the mass range of [1–1000] $M_\odot$ considering no mass-loss and have also discussed chances of the observability of an individual Pop III star. In a recent work, Murphy et al. (2021) have studied a grid of Pop III models having masses in the range of [1.7–120] $M_\odot$ and explored the effect of changing the initial rotational velocity from 0 per cent to 40 per cent of critical rotational velocity.

Taking such studies one step further, in this work, we study the entire evolution (from ZAMS up to the stage of the onset of core collapse) of a 25 $M_\odot$ Pop III star and investigate the effect of rotation on the final fates. Following the phase diagram in Yoon et al. (2012), the resulting SNe from a 25 $M_\odot$ ZAMS star will either be weak Type II or Type Ib/c depending upon the initial rotations. For the first time in this work, we have evolved the rotating and non-rotating Pop III models together up to the stage of the onset of core collapse and further performed the hydrodynamic simulations of their synthetic explosions showing the light curves of resulting transients.

We have divided the entire letter into four sections. After providing a brief introduction of literature in Section 1, we discuss the numerical set-ups and physical properties of the models in Section 2. The numerical set-ups to simulate the hydrodynamic explosion of models are discussed in Section 3. Finally, the major outcomes from the entire evolutions of the models along with their synthetic explosions are discussed in Section 4. In this section, we also provide the implications and discussions of the simulation results presented in the underlying work.

2 STELLAR EVOLUTION USING MESA

2.1 Numerical set-ups

We employ one of the state-of-the-art and 1D stellar evolution codes,MESA to perform the stellar evolutions of 25 $M_\odot$ ZAMS stars with zero metallicity ($Z = 0.00$) and different initial rotations. In this simulation work, we have utilized theMESA version r22.05.1 (Paxton et al. 2011, 2013, 2015, 2018). We start with a non-rotating, zero metallicity model and increase the angular rotational velocity (Ω) in units of 0.2 times the critical angular rotational velocity ($\Omega_{\rm crit}$) up to $\Omega/\Omega_{\rm crit} = 0.8$. Following Paxton et al. (2013), the critical angular rotational velocity is expressed as $\Omega^2_{\rm crit} = (1 - L/L_{\rm edd})GM/R^3$, where $L_{\rm edd}$ is the Eddington luminosity. As specified in the default MESA set-ups, when the ratio of the luminosity from nuclear processes and the overall luminosity of the model at a particular stage reaches 0.4 (set by `Lnuc_div_L_zams_limit` = 0.4 in MESA), the model is assumed to have reached ZAMS. Adopting the Ledoux criterion, convection is modelled utilizing the mixing theory of Henyey, Vardya & Bodenheimer (1965). We have adopted a mixing-length-theory parameter ($\alpha_{\rm MLT}$) = 2.0 in the whole analysis. Following Langer, El Eid & Fricke (1985), semiconvection is modelled by setting an efficiency parameter of $\alpha_{\rm sc} = 0.01$. To model the thermohaline mixing, we follow Kippenhahn, Ruschenplatt & Thomas (1980) by fixing the efficiency parameter to $\alpha_{\rm th} = 2.0$. In order to model the convective overshooting, we use the diffusive approach as presented in Herwig (2000) and set $f = 0.004$ and $f_0 = 0.001$ for all convective cores and shells. The stellar winds from rotating Pop III stars are also theorized to make contributions to the enrichment of the early universe with heavy metals, so, to model the stellar winds of the Pop III stars in our study, we use the 'Dutch' wind scheme (Glebbeek et al. 2009) and set the scaling factor (η) to 0.5. This

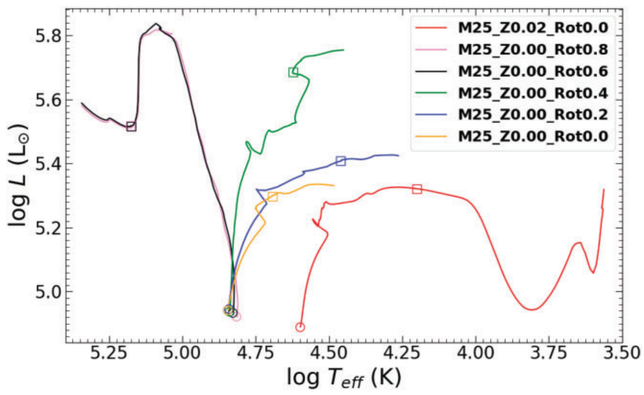

Figure 1. Evolution of the Pop III models having different rotations on the HR diagram. The arrivals of the models on ZAMS are shown by hollow circles while the core-He exhaustion stages of the models have been marked by hollow squares. The solar metallicity ($Z = 0.02$) model evolutionary track has also been shown for comparison.

wind scheme incorporates the outcomes from multiple works for different situations. With $m_{\rm H}$ representing the surface mass fraction of hydrogen, (a) when the effective temperature, $T_{\rm eff} > 10^4$ K along with $m_{\rm H}$ being greater than 0.4, the outcomes of Vink, de Koter & Lamers (2001) are used; (b) when $T_{\rm eff} > 10^4$ K combined with the $m_{\rm H}$ being lesser than 0.4, the results of Nugis & Lamers (2000) are used; and finally (c) the wind scheme presented in de Jager, Nieuwenhuijzen & van der Hucht (1988) is used in MESA for the condition with $T_{\rm eff} < 10^4$ K.

Starting from the pre-ZAMS, the 1D stellar evolutions of the Pop III models are performed till they reach the stage of the onset of the iron core collapse. The onset of core collapse is marked when the infall velocity of the iron core exceeds the specified iron core infall velocity limit of 100 km s^{-1} (set by `fe_core_infall_limit = 1d7` in MESA). In this work, the models have been named in a way that they contain the pieces of information including the ZAMS mass, metallicity (Z), and rotation ($\Omega/\Omega_{\rm crit}$ indicated by 'Rot'). For example, the model M25_Z0.00_Rot0.0 indicates a 25 $M_\odot$ ZAMS star with $Z = 0.00$, and $\Omega/\Omega_{\rm crit} = 0.0$. For comparison purposes, we have also performed the evolution of a solar metallicity ($Z = 0.02$) model with the same ZAMS mass of 25 $M_\odot$.

2.2 Physical properties of the models

Fig. 1 displays the evolutions of Pop III models with 25 $M_\odot$ ZAMS mass each, on the Hertzsprung–Russell (HR) diagram along with a similar ZAMS mass model having solar metallicity ($Z = 0.02$) for comparison purposes. Compared to a solar metallicity model, the Pop III models reach the ZAMS at higher effective temperatures ($T_{\rm eff}$) but show nearly similar ZAMS luminosities. Thus, the Pop III models are bluer than the solar metallicity model. Among Pop III models, at ZAMS, the models with higher initial angular rotational velocities possess lower luminosities and lower effective temperatures; a well-known effect of rotation as mentioned in Ekström et al. (2008). It is also evident from this figure that beyond ZAMS, the models with higher initial angular rotational velocities possess higher luminosities and higher effective temperatures as well for most of their evolutionary paths. Similar results were also obtained in the case of Yoon et al. (2012).

Fig. 2 shows the variations of $\Omega/\Omega_{\rm crit}$ and corresponding mass-loss rates ($\log|\dot{M}|$) as the models evolve up to the stage of the onset of core collapse. Initially, the models touch the specified

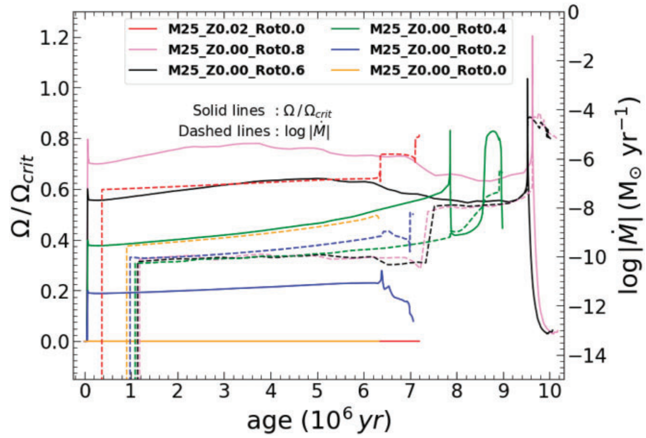

Figure 2. The evolution of angular rotational velocity (Ω) in units of critical angular rotational velocity ($\Omega_{\rm crit}$) along with corresponding mass-loss rate ($\log|\dot{M}|$) evolution.

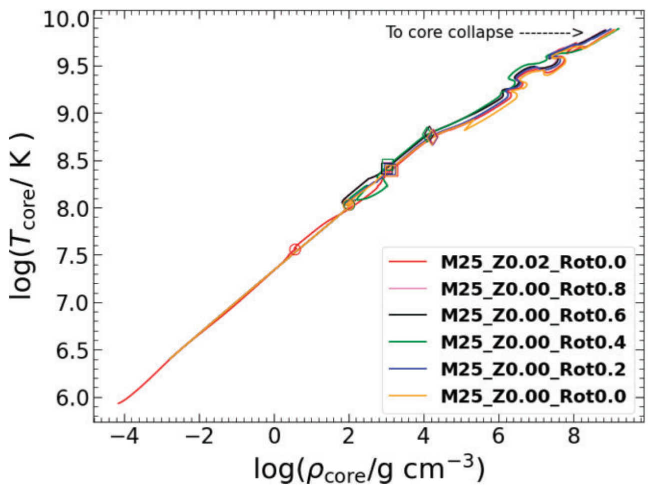

Figure 3. The variations of core-temperature ($T_{\rm core}$) versus core-density ($\rho_{\rm core}$) curves throughout the course of evolution of the models on the HR Diagram. The arrival on the ZAMS, exhaustion of core-He burning, and exhaustion of core-C burning have been marked by hollow circles, squares, and diamonds, respectively.

$\Omega/\Omega_{\rm crit}$ values and then settle to new $\Omega/\Omega_{\rm crit}$ values as they evolve further. This shows that a perturbation imposed on an equilibrium model experiences a transient response before the system settles into a new equilibrium configuration. During the last evolutionary stages, the rapidly rotating models (with $\Omega/\Omega_{\rm crit}$ = 0.6 and 0.8) show chaotic rotations exceeding the critical rotational velocities which are responsible for the dynamic events to occur as indicated by corresponding heavy mass-loss rates during these phases. Our rapidly rotating massive Pop III stars dredge up a large amount of CNO elements up to the surface during the core-He burning stage. It dramatically increases the surface metallicity, which eventually strongly boosts the radiative mass-loss through a mechanism similar to that discussed in Hirschi (2007). Thus, the rapidly rotating models are significantly stripped compared to the slow- or non-rotating models. We have also shown the Kippenhahn diagram for one slow-rotating model (M25_Z0.00_Rot0.2) and one rapidly rotating model (M25_Z0.00_Rot0.8) in Fig. A1. A few more important physical properties including radii and effective temperatures ($T_{\rm eff}$) at various stages are listed in Table 1.

The overall variations of the $\rho_{\rm core}$ versus $T_{\rm core}$ curves for the entire evolutions of the models up to the onset of core collapse are shown in Fig. 3. The arrival of the models on ZAMS, the exhaustion of core-He burning phases, and the exhaustion of core-C burning stages have been indicated by the hollow circles, squares, and diamonds, respectively. Compared to a solar metallicity model, the Pop III models ignite the H-burning in their respective cores at higher $\rho_{\rm core}$ and $T_{\rm core}$, which is due to the lack of CNO elements in Pop III stars needed to ignite the CNO cycle (Ekström et al. 2008). During the last evolutionary stages, all the models have exceeded the core temperatures of $\sim 10^{9.9}$ K; the perfect condition for the cores to collapse under their own gravity. Thus, the models have now reached the stage of the onset of core collapse.

3 SYNTHETIC EXPLOSIONS USING SNEC

Once the models have reached the stage of core collapse marked by the infall velocity exceeding the specified iron core infall velocity, the outputs of MESA in appropriate forms are provided as input to SNEC (Morozova et al. 2015). SNEC is a 1D Lagrangian hydrodynamic code that simulates the synthetic explosions of the stellar models at the stage of the onset of their core collapse. SNEC solves the radiation energy transport equations within the flux-limited diffusion approximation to simulate the explosions.

Further, in this work, to simulate the synthetic explosions of the models which have already arrived at the stage of the onset of core collapse, we closely follow the set-ups of Ouchi & Maeda (2019) along with Aryan et al. (2021, 2022) for SNEC. However, the major changes are summarized here. First, for each model, the innermost mass $M_{\rm c}$ representing the mass of the central remnant is excised before the explosion by assuming that the model will finally collapse to form a neutron star. The central remnant mass is decided by the final mass of the iron core when the model has reached the stage of the onset of core collapse. Further, a set of 800 grid cells are used to simulate the synthetic explosion of the model. With 800 grid cells, the light curves and photospheric velocities of the resulting SN from simulations are very well converged in the interested domains of time. The explosion of each model is simulated as `thermal bomb` by adding $E_{\rm exp}$ amount of energy for a duration of 0.1 s in the inner 0.1 $M_\odot$ section of the model. As discussed in Morozova et al. (2015), SNEC lacks nuclear-reaction network thus the synthesized amount of nickel (^{56}Ni) in an SN is decided, and fixed by the individual user. For each model, an amount of ^{56}Ni specified by corresponding $M_{\rm Ni}$ in Table 1, is distributed between the excised central remnant mass ($M_{\rm c}$) cut and the chosen mass coordinate which is close to the outer surface of the selected model. For models with $\Omega/\Omega_{\rm crit} \leq 0.4$, the amount of ^{56}Ni is set to 0.001 $M_\odot$ while the remaining models with heavy rotations and suffering significant mass-losses, the amount of ^{56}Ni is set to 0.05 $M_\odot$. Choosing a slightly greater amount of $M_{\rm Ni}$ for stripped models is followed by Afsariardchi et al. (2021). The ejecta mass ($M_{\rm ej}$) for each CCSN is estimated by finding the difference between the pre-SN mass ($M_{\rm pre\text{-}SN}$) and $M_{\rm c}$. The detailed explosion parameters are listed in Table 1.

Finally, the *UBVRI*-band light curves generated through synthetic explosions are shown in Fig. A2. As shown in this figure, the slow-rotating models (i.e. models M25_Z0.00_Rot0.0, M25_Z0.00_Rot0.2, M25_Z0.00_Rot0.4, and the solar metallicity model M25_Z0.02_Rot0.0) retaining a significant amount of their outer H-envelope result into Type II CCSNe while the rapidly rotating models result into CCSNe Type Ib/c. These results are also complementing the results as predicted in the phase diagram of Yoon et al. (2012) in fig. 12. In Fig. A2, a few important simulation results

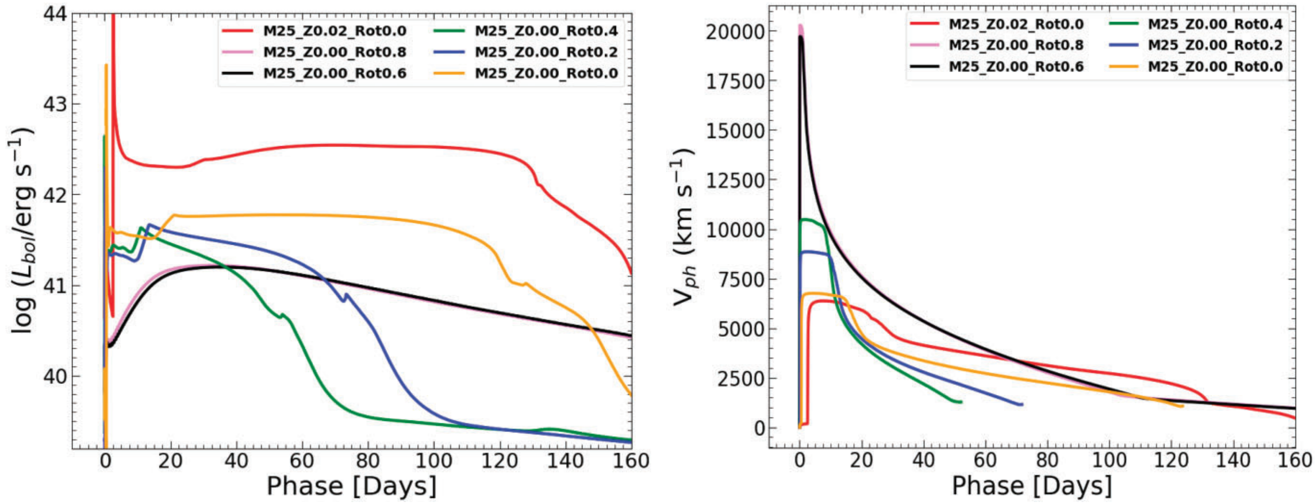

Figure 4. *Left:* The bolometric luminosity light curves resulting from the synthetic explosions of models using SNEC. *Right:* corresponding photospheric velocity evolutions. Results of the non-rotating, solar metallicity model are also shown for comparison.

Table 1. The ZAMS and pre-SN properties of the Pop III models using MESA along with the SNEC explosion parameters.

	ZAMS				Pre-SN				Explosion			
Model name	$M^a_{\rm ZAMS}$ (M$_\odot$)	$T_{\rm eff}$ (K)	$R^b_{\rm ZAMS}$ (R$_\odot$)	$L^c_{\rm ZAMS}$ (L$_\odot$)	$M^d_{\rm Pre-SN}$ (M$_\odot$)	$T_{\rm eff}$ (K)	$R^e_{\rm Pre-SN}$ (R$_\odot$)	$L^f_{\rm pre-SN}$ (L$_\odot$)	$M^g_{\rm c}$ (M$_\odot$)	$M^h_{\rm ej}$ (M$_\odot$)	$M^i_{\rm Ni}$ (M$_\odot$)	$E^j_{\rm exp}$ (10^{51} erg)
M25_Z0.00_Rot0.0	25.0	70069	2.01	4.94	24.99	10 319	195	5.58	1.70	23.29	0.001	1.0
M25_Z0.00_Rot0.2	25.0	69877	2.02	4.94	24.99	17 216	57	5.42	2.00	22.99	0.001	1.0
M25_Z0.00_Rot0.4	25.0	68882	2.07	4.94	24.96	29 784	32	5.87	1.80	23.16	0.001	1.0
M25_Z0.00_Rot0.6	25.0	67069	2.16	4.93	11.94	140 668	1.5	5.90	2.10	9.84	0.05	1.0
M25_Z0.00_Rot0.8	25.0	65107	2.26	4.91	11.79	175 858	0.6	5.53	2.10	9.69	0.05	1.0
M25_Z0.02_Rot0.0	25.0	3962	5.91	4.88	22.64	3623	1219	5.36	1.90	22.74	0.001	1.0

[a]Mass at ZAMS. [b]Progenitor radius at ZAMS. [c]Luminosity at ZAMS. [d]Final mass of pre-SN model. [e]Pre-SN phase radius. [f]Pre-SN phase luminosity. [g]Mass of the central remnant in simulation. [h]Ejecta mass. [i]Amount of synthesized nickel used in the explosion. [j]Explosion energy.

of the H-rich Pop III CCSNe (i.e. models with $\Omega/\Omega_{\rm crit} \leq 0.4$) are also displayed. First, the peak magnitudes of the shock breakout (SBO) features from these models are much fainter than a typical solar metallicity H-rich CCSN; secondly, the absolute magnitudes of the plateau of the H-rich Pop III CCSNe are at least 1.5 mag fainter than the solar metallicity H-rich CCSN, thus the H-rich Pop III CCSNe are pretty faint within the considered limits of $E_{\rm exp}$ and $M_{\rm Ni}$ in this study. The effect of bolometric light curves becoming less luminous as metallicity decreases has been explored in Kasen & Woosley (2009) and Paxton et al. (2018). The primary cause of this behaviour is associated with the smaller pre-SN radius and less total mass-loss as an effect of lower metallicity. However, in their work, they have not calculated the light curves corresponding to $Z = 0.00$; and thirdly, surprisingly, although the pre-SN radius of the non-rotating H-rich Pop III model is much smaller than a non-rotating solar metallicity H-rich model, the earlier model shows almost a similar plateau duration. The non-rotating solar model has a larger pre-SN radius compared to the M25_Z0.00_Rot0.0 model, but the latter has a more massive H-envelope. From Fig. A3, the M25_Z0.02_Rot0.0 model has an H-envelope starting from a mass coordinate, $m({\rm M}_\odot) \sim 8\,{\rm M}_\odot$ while the M25_Z0.00_Rot0.0 has a more massive H-envelope starting from $m({\rm M}_\odot) \sim 5\,{\rm M}_\odot$. Thus, the presence of extra hydrogen could be responsible for the increased plateau duration in the non-rotating Pop III model. Finally, the rapidly rotating H-less Pop III models result into much fainter Type Ib/c SNe. These explosions are fainter because of the less explosion energy (and an $M_{\rm Ni}$ of $0.05\,{\rm M}_\odot$) considered in our study. With higher explosion energies and more nickel production, they might result in more luminous SNe or hypernovae (Nomoto, Kobayashi & Tominaga 2013). SNEC could also produce the bolometric luminosity light curves and the corresponding photospheric velocity evolutions for all the models as shown in the left-hand and the right-hand panels of Fig. 4, respectively. In the left-hand panel, the bolometric light curves of the Pop III CCSNe display a similar behaviour as earlier in the case of *UBVRI*-band light curves comparison with the solar metallicity model. In the right-hand panel, as expected, the stripped models display higher photospheric velocities compared to the H-rich models.

4 RESULTS AND DISCUSSION

In this work, we have performed the 1D stellar evolutions of Pop III models up to the stage of the onset core collapse and then simulated their synthetic explosions. Utilizing the 1D simulations performed in this work, we summarize our findings below:

(i) The peak absolute magnitudes of the SBO features of Pop III CCSNe are much smaller than that of a CCSN resulting from a solar Type model with similar ZAMS mass.

(ii) The H-rich CCSNe from Pop III models are fainter than the H-rich SN resulting from a solar metallicity model. The plateau magnitudes of Pop III star H-rich CCSNe are at least 1.5 mag fainter than the latter. In the earlier epochs, the stripped CCSNe from Pop

III models are much fainter than SNe resulting from H-rich Pop III models.

(iii) One of the most intriguing results from our simulations is that although the pre-SN radius of a non-rotating H-rich Pop III model is much smaller than a non-rotating H-rich solar Type model, both models show nearly similar plateau durations. One of the reasons for the increased plateau duration despite a relatively smaller pre-SN radius in non-rotating Pop III CCSNe could be associated with the increased amount of hydrogen mass.

(iv) Among the discussed Pop III models, SN resulting from the non-rotating H-rich model is the brightest. It has a nearly constant absolute magnitude of around −16.5 mag in the *V*-band for the plateau phase. This would correspond to an apparent magnitude of ∼35.5 mag at a redshift of $z = 10$ (using the cosmology of a Hubble constant, $H_0 = 73$, $\Omega_{\rm M} = 0.3$, and $\Omega_{\rm vac} = 0.7$). Currently, no ground- or space-based observatory can go this faint to detect a Pop III CCSN resulting from an individual star however with the major advancement in observational technologies having large diameters could possibly detect such events in near future.

(v) Thus, through our work, we find that within the considered limits of explosion energies and nickel masses, these transient events are very faint, making it difficult for them to be detected at high-redshifts.

ACKNOWLEDGEMENTS

The authors are highly thankful to the anonymous referee for providing constructive comments for the significant improvement of the letter. AA duly acknowledges the supports furnished by CSIR, India [under the file no. 09/948(0003)/2020-EMR-I]. AA also sincerely acknowledges useful discussions and suggestions received from MESA user community with special thanks to Prof. Francis Timmes. SBP and RG acknowledge the support of ISRO provided under the AstroSat archival data utilization program [DS_2B-13013(2)/1/2021-Sec.2].

DATA AVAILABILITY

The `inlist` files for MESA simulations and SNEC input files will be uploaded to `zenodo` publicly. One can download those files to reproduce the simulation results.

REFERENCES

Abel T., Bryan G. L., Norman M. L., 2002, Science, 295, 93
Abia C. I., Straniero O., Limongi M., Chieffi A., Isern J., 2001, ApJ, 557, 126
Afsariardchi N. M. R., Khatami D. K., Matzner C. D., Moon D.-S., Ni Y. Q., 2021, ApJ, 918, 89
Aryan A. et al., 2021, MNRAS, 505, 2530
Aryan A. et al., 2022, MNRAS, 517, 1750
Barkana R. A., 2001, Phys. Rep., 349, 125
Bromm V., 2013, Rep. Prog. Phys., 76, 112901
Bromm V., Coppi P. S., Larson R. B., 1999, ApJ, 527, L5
Brook C. B., Kawata D., Scannapieco E., Martel H., Gibson B. K., 2007, ApJ, 661, 10
Chiaki G., Susa H., Hirano S., 2018, MNRAS, 475, 4378
Ciardi B., Ferrara A., Marri S., Raimondo G., 2001, MNRAS, 324, 381
Clark P. C., Glover S. C. O., Smith R. J., Greif T. H., Klessen R. S., Bromm V., 2011, Science, 331, 1040
de Jager C., Nieuwenhuijzen H., van der Hucht K. A., 1988, A&AS, 72, 259
Ekström S., Meynet G., Chiappini C., Hirschi R., Maeder A., 2008, A&A, 489, 685
Ferrara A., Pettini M., Shchekinov Y., 2000, MNRAS, 319, 539
Glebbeek E., Gaburov E., de Mink S. E., Pols O. R., Portegies Zwart S. F., 2009, A&A, 497, 255
Greif T. H., Bromm V., Clark P. C., Glover S. C. O., Smith R. J., Klessen R. S., Yoshida N., Springel V., 2012, MNRAS, 424, 399
Haiman Z., Rees M. J., Loeb A., 1997, ApJ, 476, 458
Heger A., Woosley S. E., 2010, ApJ, 724, 341
Henyey L., Vardya M. S., Bodenheimer P., 1965, ApJ, 142, 841
Herwig F., 2000, A&A, 360, 952
Hirano S., Hosokawa T., Yoshida N., Umeda H., Omukai K., Chiaki G., Yorke H. W., 2014, ApJ, 781, 60
Hirano S., Hosokawa T., Yoshida N., Omukai K., Yorke H. W., 2015, MNRAS, 448, 568
Hirschi R., 2007, A&A, 461, 571
Hosokawa T., Omukai K., Yoshida N., Yorke H. W., 2011, Science, 334, 1250
Ishiyama T., Sudo K., Yokoi S., Hasegawa K., Tominaga N., Susa H., 2016, ApJ, 826, 9
Kasen D., Woosley S. E., 2009, ApJ, 703, 2205
Kippenhahn R., Ruschenplatt G., Thomas H. C., 1980, A&A, 91, 175
Kirihara T., Hasegawa K., Umemura M., Mori M., Ishiyama T., 2020, MNRAS, 491, 4387
Langer N., El Eid M. F., Fricke K. J., 1985, A&A, 145, 179
Marigo P., Chiosi C., Kudritzki R. P., 2003, A&A, 399, 617
Morozova V., Piro A. L., Renzo M., Ott C. D., Clausen D., Couch S. M., Ellis J., Roberts L. F., 2015, ApJ, 814, 63
Murphy L. J. et al., 2021, MNRAS, 501, 2745
Nakamura F., Umemura M., 2001, ApJ, 548, 19
Nomoto K., Kobayashi C., Tominaga N., 2013, ARA&A, 51, 457
Nugis T., Lamers H. J. G. L. M., 2000, A&A, 360, 227
Ouchi R., Maeda K., 2019, ApJ, 877, 92
Paxton B., Bildsten L., Dotter A., Herwig F., Lesaffre P., Timmes F., 2011, ApJS, 192, 3
Paxton B. et al., 2013, ApJS, 208, 4
Paxton B. et al., 2015, ApJS, 220, 15
Paxton B. et al., 2018, ApJS, 234, 34
Riaz R., Bovino S., Vanaverbeke S., Schleicher D. R. G., 2018, MNRAS, 479, 667
Salvadori S., Ferrara A., Schneider R., Scannapieco E., Kawata D., 2010, MNRAS, 401, L5
Silk J., 1983, MNRAS, 205, 705
Stacy A., Greif T. H., Bromm V., 2010, MNRAS, 403, 45
Stacy A., Bromm V., Lee A. T., 2016, MNRAS, 462, 1307
Tegmark M., Silk J., Rees M. J., Blanchard A., Abel T., Palla F., 1997, ApJ, 474, 1
Todini P., Ferrara A., 2001, MNRAS, 325, 726
Tumlinson J., Shull J. M., 2000, ApJ, 528, L65
Turk M. J., Abel T., O'Shea B., 2009, Science, 325, 601
Vink J. S., de Koter A., Lamers H. J. G. L. M., 2001, A&A, 369, 574
Windhorst R. A. et al., 2018, ApJS, 234, 41
Wollenberg K. M. J., Glover S. C. O., Clark P. C., Klessen R. S., 2020, MNRAS, 494, 1871
Yoon S. C., Dierks A., Langer N., 2012, A&A, 542, A113

APPENDIX A: ADDITIONAL FIGURES AND TABLES

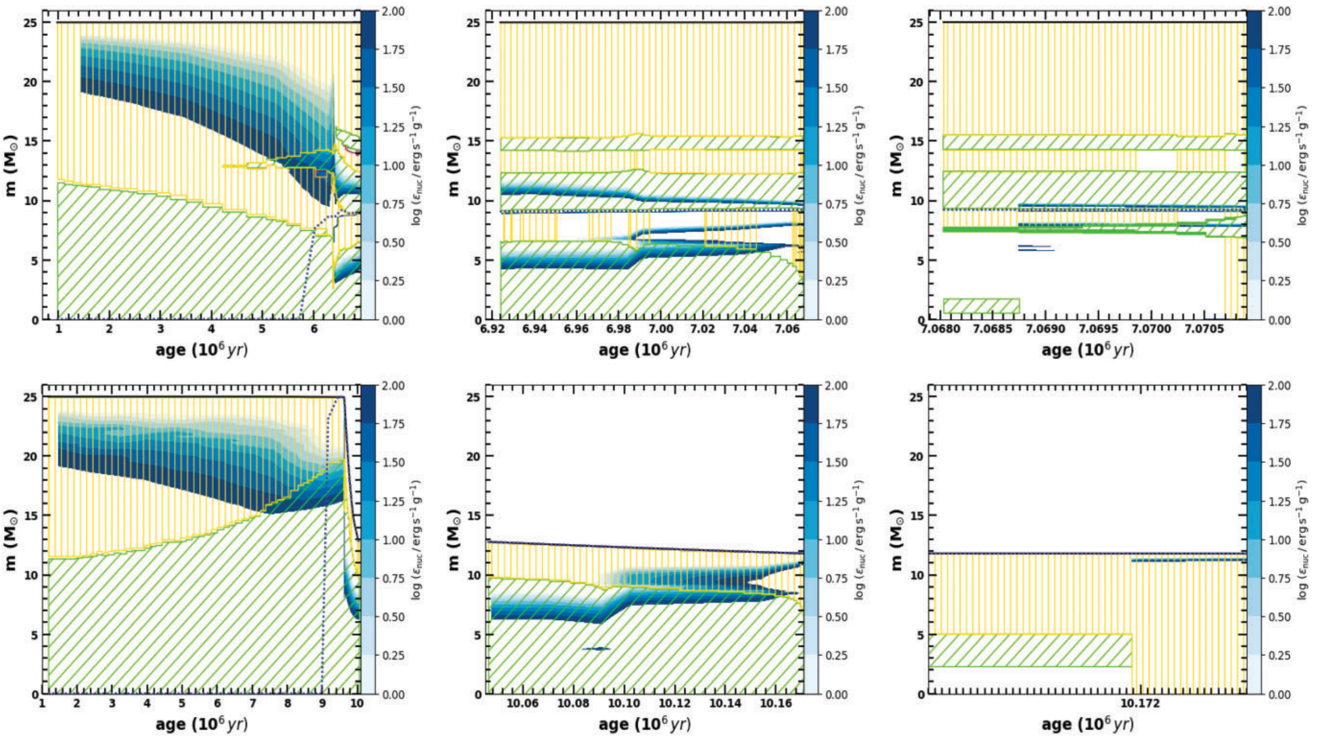

Figure A1. The Kippenhahn diagrams of the models M25_Z0.00_Rot0.2 (top) and M25_Z0.00_Rot0.8 (bottom) for a period between ZAMS to close to the pre-SN stage. Here, the green hatchings indicate the convective regions and the dark yellow regions mark the stellar interiors where the thermohaline mixing is going on. Also, the logarithm of the specific nuclear energy generation rate ($\epsilon_{\rm nuc}$) inside the stellar interiors is indicated by the blue colour gradients. The rapidly rotating model is significantly stripped.

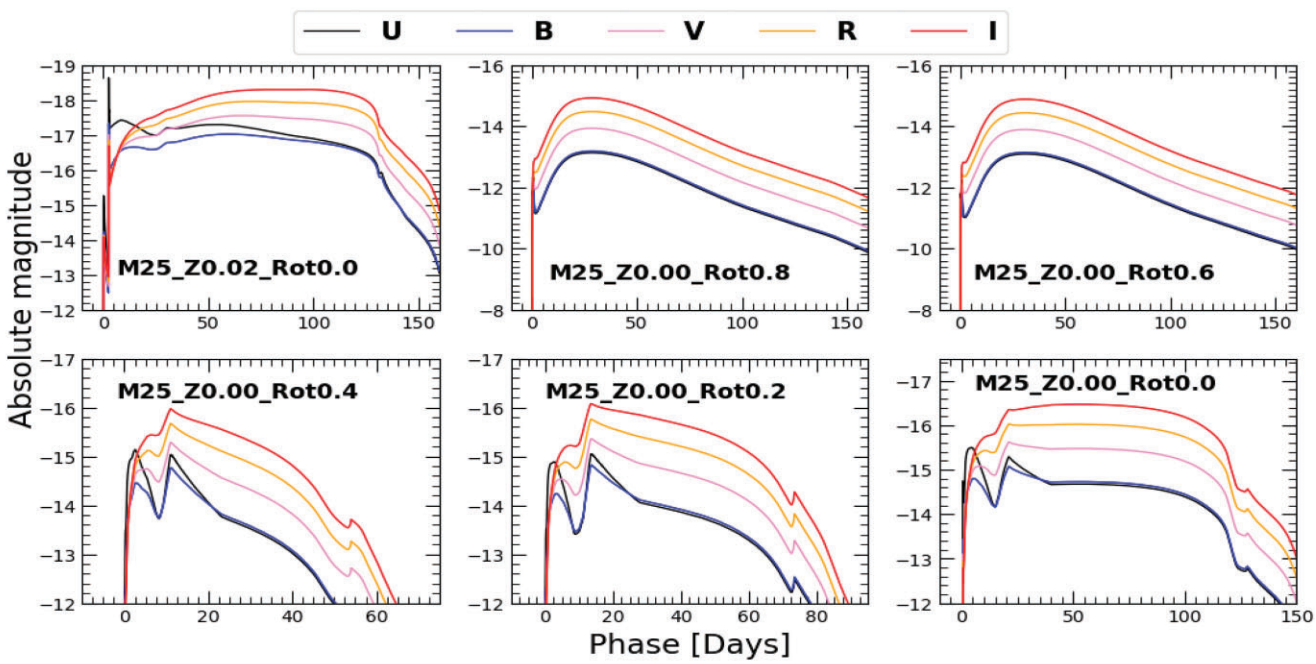

Figure A2. The *U*-, *B*-, *V*-, *R*-, and *I*-band light curves resulting from the synthetic explosions of Pop III models using SNEC. The non-rotating and slowly rotating models ($\Omega \leq 0.4\,\Omega_{\rm crit}$) form a class of weak Type II SNe, while the rapidly rotating models ($\Omega \geq 0.6\,\Omega_{\rm crit}$) result into Type Ib/c SNe within the specified limits of explosion energies and nickel masses. The light curves resulting from the non-rotating, solar metallicity model are also shown for comparison.

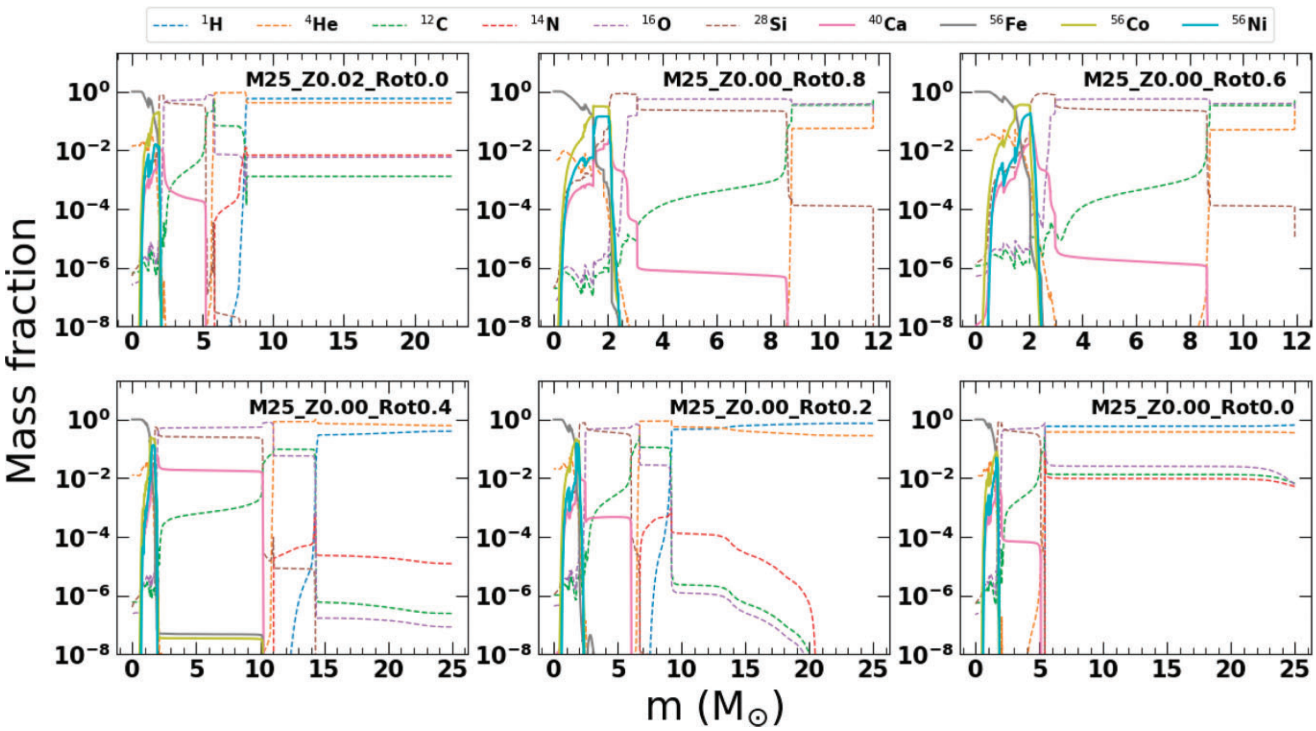

Figure A3. A combined plot showing the mass fractions of various elements for the models in this study at a stage when the models have reached the stage of the onset of core collapse.

This paper has been typeset from a TEX/LATEX file prepared by the author.